

Geophysical monitoring of a laboratory-scale internal erosion experiment

Yara Maalouf¹, Grégory Bièvre¹, Christophe Voisin¹ and Naji Khoury²

¹Université Grenoble Alpes, Université Savoie Mont-Blanc, CNRS, IRD, Université Gustave Eiffel, Grenoble, France, and ²Notre Dame University–Louaize, Zouk Mosbeh, Lebanon

Received July 2021, revision accepted May 2022

ABSTRACT

Earth dams are structures used worldwide for water management. Their failure over time is notably due to water seepage generating internal erosion. There is a growing need to detect the processes at work as early as possible. This study presents a controlled laboratory experiment aimed at detecting and monitoring water seepage into a soil sample. The experiment was monitored with electrical resistivity tomography, velocimeters and video recording. The video recording of the downstream side of the soil sample shows successive episodes of mass movements associated with a progressive water flow increase. The electrical resistivity tomography, limited by a low temporal resolution, shows an evolution of the resistivity in agreement with the evolution of the soil sample (e.g., saturation and mass movements), but with strong limitations regarding the robustness of the results. The continuous seismic recording reveals extra rupture episodes that occur inside the volume of the soil sample, which were not recorded by the video. Their distribution in time and energy illustrates strongly nonlinear changes in the soil sample, with several phases of acceleration. A controlled source monitoring using external repetitive events allows probing the medium with an enhanced temporal resolution compared to electrical resistivity tomography. The apparent seismic velocity of the soil sample reveals a nonlinear decrease, high at the beginning of the experiment, and then stalled until the different mass movements enlarge the amount of water inside the sample along with the water flow. The different techniques used, especially seismic monitoring, describe a complex and strongly nonlinear process of internal erosion centred around the coupling between water flow and internal damage. Finally, these findings suggest that seismic methods could be able to distinguish the four different phases of internal erosion (namely, initiation, continuation, progression and failure) discussed in the geotechnical literature.

Key words: Internal erosion, Piping, Laboratory Experiment, Seismic monitoring, Electrical resistivity.

INTRODUCTION

Earth dams, such as levees, embankments and dykes, have existed for centuries and are the most abundant type of dams in the world (Morales-Nápoles *et al.*, 2014). The sudden failure

and the subsequent massive release of water within a rapid timeframe (Fell *et al.*, 2003) have caused massive losses in lives and lands throughout the years (Foster *et al.*, 2000a; Silva Rotta *et al.*, 2020). Based on the available literature on dam failures and the register of dams stated in the International Commission on Large Dams database (ICOLD, 2001, 2017), 48% of failures of dams constructed between 1800 and 1986

E-mail: yara.maalouf@univ-grenoble-alpes.fr

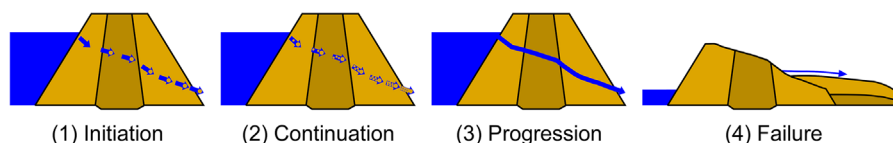


Figure 1 The different stages of internal erosion in the backward erosion type (modified from Fell *et al.*, 2015). (1) Initiation, when the first soil particle is driven downstream. (2) Continuation, when additional soil particles are washed away. (3) Progression is the formation of the pipe in the embankment. (4) The breach represents the complete failure of a part of the dam and allows the water to flow out of the reservoir.

resulted from overtopping, 6% were caused by static and seismic instability and, finally, 46% of worldwide dam failures resulted from internal erosion.

Internal erosion is defined as the process of soil particles' movement from the core of the structure towards the downstream by seepage (Terzaghi *et al.*, 1996). Statistical results showed that 31% of erosion failures were caused by piping through the embankment (Foster *et al.*, 2000a,b), which is due to the excessive seepage of water and transport of soil particles until the formation of a pipe inside the body of the structure. Moreover, the results of the study conducted by Foster *et al.* (1998) indicate that about 1 in 200 dams failed due to piping, and 1 in 60 experienced a piping incident. According to Foster and Fell (1999) and Fell *et al.* (2015), internal erosion may develop through the embankment, the foundation, and also from the embankment into (or at) the foundation. The causes of degradation of dams vary, but are mainly due to the fill material used, an increase in loading, the bad design of filters, or the improper selection of the embankment core materials.

The internal erosion and piping processes are described by different stages, the relative duration of which is unknown, as illustrated in Figure 1. The first stage, called initiation, is either related to the development of a concentrated leak, suffusion or backward erosion (Van Beek *et al.*, 2013; ICOLD, 2017). The second stage of internal erosion is called continuation. In this stage, internal erosion can be stopped if the filters are properly designed to prevent the washout of fine materials; otherwise, internal erosion will proceed to stage 3, called progression (Foster *et al.*, 2000a). It corresponds to the formation of a pipe in the body of the dam. Once the pipe is created, the internal erosion process accelerates up to the failure (stage 4; Fell *et al.*, 2003). The potential loss of lives caused by the failure of a dam relies mostly on the warning time given to evacuate areas at risk downstream of the dam (Fell *et al.*, 2003). For example, around 20 years ago, the United States Bureau of Reclamation recommended that the warning time of failure be a minimum of 60 minutes to save lives (Graham, 1999). According to Fell *et al.* (2015), internal erosion is more likely to be detected in the advanced

stages of progression and breach formation (i.e., late stage 3 and stage 4). Hence, it appears crucial to detect as early as possible an ongoing internal erosion process and identify its current stage (1, 2 or 3).

Fell and Fry (2007) proposed a three-step methodology to detect weak zones within earth dams. It consists of (1) non-destructive (among which geophysical) techniques to determine probable weak zones, (2) detailed (geophysical and geotechnical) investigation of the weak area to determine its state, and (3) undergo geotechnical testing to determine the physical properties of the soil. Beyond the identification of potential weak zones within these structures, geophysical techniques can be used to monitor their temporal evolution. Repetitive active measurements (e.g., time-lapse approach) have shown to be successful to detect and monitor leakage and seepage paths, especially using electrical resistivity tomography (ERT; Sjødahl *et al.*, 2009; Weller *et al.*, 2014). Monitoring of earth dams using active seismic methods has been poorly reported so far. These approaches require, however, periodic reinstallations of experimental setups in the field and provide only poorly constrained temporal resolution (see, discussion by Hirose *et al.*, 2017). An alternative is to perform continuous monitoring of the structure. This can be achieved using permanently installed devices, which have been mainly reported for ERT so far (Gunn *et al.*, 2018). Continuous passive seismic recordings allow monitoring of the structure and its evolution by detecting seismic events that reflect the changes and reorganizations of the internal structure. A study conducted by Rittgers *et al.* (2015) on the IJkdijk experimental field dam (the Netherlands) showed the ability of self-potential combined with passive seismic monitoring to detect, localize and monitor changes in porous media. The acoustic events (AE) detected in the passive seismic monitoring were isolated and arrival times were obtained and used to localize the source of these events in the dam. A geophysical study was conducted on a real dyke in France using, among others, seismic techniques (Bièvre *et al.*, 2017). This study showed increases in seismic amplitudes recorded by a group of 4 geophones (over a spread of 24 located on the crest of

the dyke) located above a seepage zone. The impulsive signals were also used to successfully locate at 3.4 m depth a 0.2–0.3 m wide seepage zone within the dyke. After remediation works, no high amplitude nor impulsive signals were observed.

Additionally, seismic noise can be turned into a tool for monitoring seismic velocity variations at various scales (from the Earth's crust to laboratory experiments) through cross-correlation of successive time windows. As water affects the seismic wave velocity, the application of seismic noise interferometry to groundwater monitoring has been used to detect changes in the water table (Voisin *et al.*, 2016; Clements and Denolle, 2018; Garambois *et al.*, 2019). Planès *et al.* (2016) reported the seismic monitoring of a 6-m-long and 0.6-m-high canal embankment made of silty sand. They introduced a 1.3 cm diameter metal rod in the embankment that was pulled out to initiate the piping process (i.e., the experiment started directly at internal erosion stage 3, namely progression; Fig. 1). They recorded semi-continuously the ambient noise with 10 vertical geophones. Using seismic interferometry, they monitored a wave velocity drop of 20% and further interpreted it as originating from a structure modification associated with an increase in the water flow. Using the same methodology on a real site, Olivier *et al.* (2017) were able to detect velocity variations down to -2% that they related to a local increase in water level in the dam.

The main objective of this work is to capture the complete process of internal erosion, from the generation of water seepage until failure. For this, a laboratory experiment was designed in which water is forced to pass into a cylindrical soil sample held into a concrete beam. The ability of 2D ERT to detect changes with this particular setup was first evaluated numerically. ERT and passive seismic monitoring data (event detection and correlation) were then processed, and the obtained time series are eventually interpreted in reference to internal erosion.

MATERIALS AND METHODS

Many laboratory experiments devoted to the study of internal erosion consist in building small-scale earth dams contained in tanks and encompassing artificial defects (Planes *et al.*, 2016). However, in this configuration, water leakage may develop at the interface between the earth dam and the tank. These water leakages at the interfaces may be much more important than the one developing in the artificial weak zone. Furthermore, they prevent the detection of weak seismic signals that could correspond to early stages of internal erosion. To avoid

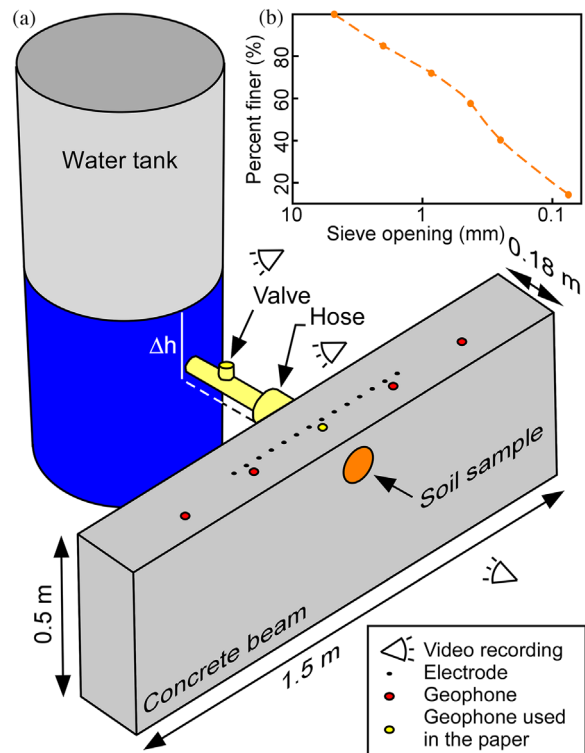


Figure 2 (a) Laboratory setup of the seepage experiment. Δh represents the difference in water height between the water level in the tank and the bottom of the soil sample zone. (b) The granulometric distribution of the soil sample is shown.

this issue, it was then decided to force a constant head of water to flow only in a weak zone, made here of a cylindrical soil sample embedded into a concrete beam. The system was then left to evolve naturally from progressive saturation up to failure.

Experimental setup

The laboratory setup consists of a plexiglass tank for water storage, a concrete beam and a hose as schematized in Figure 2. The plexiglass tank has a diameter of 0.5 m and a height of 1.25 m and serves as a water supply to the system. The beam shown in Figure 2 consists of concrete mixed at a low water-to-cement ratio (0.53) to increase its strength. A cylindrical hole 0.1 m in diameter was intentionally left to insert the soil specimen. The tank is connected to the seepage zone in the concrete beam through a PVC pipe. A valve controls the water flow. Three cameras were also used to monitor the experiment (rate of 30 frames per second). One camera was placed on the tank to monitor the water

level. The two others were placed apart from the soil sample (i.e., upstream and downstream) to time-stamp the observed events.

Geotechnical characteristics of the seepage zone

Soil erodibility controls the duration of any internal erosion test. The soil sample was devised as a mixture of sand and clay. A mixture of 65% sand and 35% of lean clay was chosen. The sand was passed through sieve no. 4 (4.75 mm opening). The sieve analysis was conducted according to international standard D6913 (ASTM, 2017). The granulometric distribution in Figure 2 shows that the soil is sandy clay with more than 50% retained on the 0.075 mm opening sieve. The sample was mixed at the optimum moisture content (OMC) of 11.3%. The erosion rate index of the soil sample was evaluated following the hole erosion test (Wan and Fell, 2004). It presents a value of 2, which corresponds to a very rapid erosion with a duration between initiation and failure lower than 3 h after Fell *et al.* (2003). The soil was then compacted inside the concrete beam, perpendicular to the flow (which is not the conventional compaction method with respect to the direction of the water flow in a real earth dam, but it does not cause a problem during the experiment), in 5 layers of 400 g each using a wood piece to a height of 3.6 cm leading to a dry density of 13.49 kN/m³.

Before the beginning of the experiment, the soil sample (prepared at its OMC of 11.3%) is not saturated with water. The experiment started by filling the tank with water at the desired height to reach the targeted hydraulic gradient. The valve was then opened to place the water in contact with the soil sample. From this time, the experiment evolved naturally without any external forcing. Under these experimental conditions, the time to failure of the soil sample is controlled only by the hydraulic gradient i (dimensionless) with respect to the critical hydraulic gradient i_c . Piping is initiated when i equals or is greater than i_c (Terzaghi *et al.*, 1996), where i is defined as:

$$i = \frac{\Delta h}{L}, \quad (1)$$

where Δh is the head difference of water between the upstream and the downstream (m), and L is the length of the soil specimen (0.18 m in the experiment). The critical hydraulic gradient i_c (dimensionless) reads as:

$$i_c = \frac{\gamma'}{\gamma_w} = \frac{G_s - 1}{1 + e}, \quad (2)$$

where γ is the submerged unit weight of soil (kN/m³), γ_w is the unit weight of water (kN/m³), G_s is the specific gravity, and e is the void ratio (both dimensionless).

The specific gravity G_s was determined using standard D854 (ASTM, 2014) and was estimated to be 2.66 ± 0.01 . The void ratio was estimated to $e = 0.93 \pm 0.01$, leading to a critical hydraulic gradient i_c of 0.86 ± 0.01 . Given the length of the soil sample of 18 cm, the critical head H_c to be used to initiate internal erosion is 15.48 cm. A height of 15.5 cm was then chosen for the experiment. Given the large diameter of the water tank (50 cm), the hydraulic gradient is maintained slightly above the critical value throughout the experiment to ensure the eventual failure of the soil sample. The latter is controlled primarily by the hydraulic gradient, but also by the soil compaction. Three preliminary feasibility tests were performed under the chosen experimental conditions and soil sample properties. They aimed at evaluating the time to failure, and the mode of failure (sudden or with intermediary mass movements). They showed times of failure between 5 min and 10 min, with an average of 7.6 ± 1.8 min.

Electrical resistivity tomography

Electrical resistivity represents the ability of a material to oppose the flow of electrical current. Apparent electrical resistivity is measured using a quadrupole with two current-injecting electrodes and two other electrodes to measure the induced voltage. The measured resistance R (Ω) is multiplied by a geometric factor K (m) to obtain the apparent electrical resistivity ρ_a ($\Omega \cdot m$). Fourteen electrodes were linearly spread with a regular spacing of 5 cm on the top of the concrete beam (Fig. 2). The centre of this 0.65-m-long profile was positioned above the soil sample. Holes were drilled to a depth of 1.0 cm on the top of the concrete beam of the same diameter as the steel electrodes inserted (0.5 cm). Holes were filled with a saltwater solution to decrease contact resistance as much as possible. Electrodes were connected to a single-channel AGI SuperSting resistivity meter (Advanced Geosciences, Inc.).

A dipole–dipole (DDP) configuration array was chosen for the measurements. An average DDP sequence with 14 electrodes and a spacing multiplication factor interval up to 5 includes 74 direct measurements. Adapting the delay and measurement times leads, with the device, to a duration of around 10 min for the whole sequence. After the feasibility tests, the time to failure of the soil sample (around 8 min) required the definition of a resistivity measurement sequence much shorter than 10 min to get several sequences during the experiments gaining, however, sufficient resolution. This was

achieved using the forward-modelling F3DM package (Clément and Moreau, 2016). Forward modelling was conducted using a methodology already applied to earth dykes (Bièvre *et al.*, 2018). Succinctly, the 3D mesh was built with the Comsol Multiphysics software and resulted in around 23,000 tetrahedrons with a maximum volume of $1.5 \times 10^{-4} \text{ m}^3$ in the concrete. The resistivity of the concrete and the soil sample at its OMC was measured (500 $\Omega\cdot\text{m}$ and 300 $\Omega\cdot\text{m}$, respectively). These values were further used for forward computations, to use realistic parameters. Since moderate resistivity variations are expected, only one configuration was used for forward computing, namely the concrete (500 $\Omega\cdot\text{m}$) and the soil zone at its optimum moisture content (300 $\Omega\cdot\text{m}$). Different configurations with reduced measurements were generated and computed using a trial-and-error approach. For a matter of time of acquisition, only direct measurements were considered. Considering the initial sequence had a limited amount of measurements (74), a manual reduction of measurements was conducted, keeping the ones located in the area of the soil sample zone on the pseudo-section. The results were compared in terms of coverage with respect to the initial sequence made of 74 measurements (further referred to as the complete sequence). The optimized sequence providing the highest coverage in the soil sample zone was eventually selected. Finally, it must be stressed that the objective of ERT is not to image the soil zone, but rather to monitor changes with time.

Measured apparent resistivity data were inverted using the BERT package (Günther *et al.*, 2006; Rücker *et al.*, 2006) with a custom 3D mesh made of around 17,500 tetrahedrons. The goal of inversion is to provide a model depicting the spatial distribution of resistivity and that satisfactorily fits the experimental apparent resistivity data. Although measurements were conducted in 2D, 3D inversion was preferred to take into account the particular geometry of the experiment with small dimensions and a finite domain. Variations of coupling between the electrodes and the concrete during experiments did not allow to consider a homogeneous resistivity for the concrete during the time-lapse experiment. Consequently, the resistivity of the concrete could not be set homogeneous during inversion. However, considering that most changes should occur in the soil sample zone, smoothness decoupling was used between the two zones (50% decoupling). Time-lapse data were inverted using different strategies: individual inversion and also ratio and difference inversion. The best results were obtained using the difference inversion (LaBrecque and Yang, 2001) using the model representing the initial dataset as a starting reference for subsequent time steps. Results were evaluated in terms of reconstruction of the resistivity distri-

bution and of statistical results, such as χ^2 and relative root mean square error (RRMSE, in %). For analysing the evolution of resistivity, the averages were computed using an individual weighting of each cell in the model in terms of volume and coverage (details in Bièvre *et al.*, 2021).

Seismic monitoring

The preliminary intent of the seismic monitoring of the experiment is to reveal potential seismic activity related to either the water flow inside the soil sample, together with small cracks or seismic signals associated with grain rearrangements, mass movements or failures. Seismic data were acquired using 5 vertical geophones of 4.5 Hz nominal frequency. The spacing between the geophones was 30 cm with the third geophone placed above the seepage zone (Fig. 2). Data were acquired continuously during the experiment with a sampling frequency of 500 Hz. Since seismic velocities in concrete are elevated (P-wave velocity above 2000 m/s), information obtained by the 5 geophones showed to be redundant and only the results from the geophone placed above the soil zone will be further presented. Passive monitoring of the experiment was conducted by recording waves propagating inside the experiment and detecting small seismic events. The acoustic emission introduced by Koerner *et al.* (1981) on dams consists of counting seismic events with amplitudes larger than a certain threshold. This has been used to monitor earth dams and to detect changes occurring inside the structure (Rittgers *et al.*, 2015). In the present work, seismic signals were filtered in different frequency ranges and normalized to the maximum amplitude of a 5-min-long time window of the signal during the water flow in the soil sample. Following the normalization, different thresholds were set and the peaks exceeding the thresholds were cumulated and normalized by their maximum. These time series were then compared to events detected in the video monitoring in order to identify the different stages of internal erosion.

Ambient seismic noise monitoring is a technique that consists of correlating seismograms of different geophones in order to identify relative changes in velocity (dV/V) and/or in the correlation coefficient (cc) of the waves. Ambient noise mainly consists of surface waves propagating in the presence of a free boundary, and the velocity of which depends on the frequency (Foti *et al.*, 2018). The velocity of surface waves depends on the elastic property of the sub-surface, among which the shear-wave velocity is the main controlling property. Changes in velocity are related to changes in stiffness while changes in cc are related to geometrical or structural

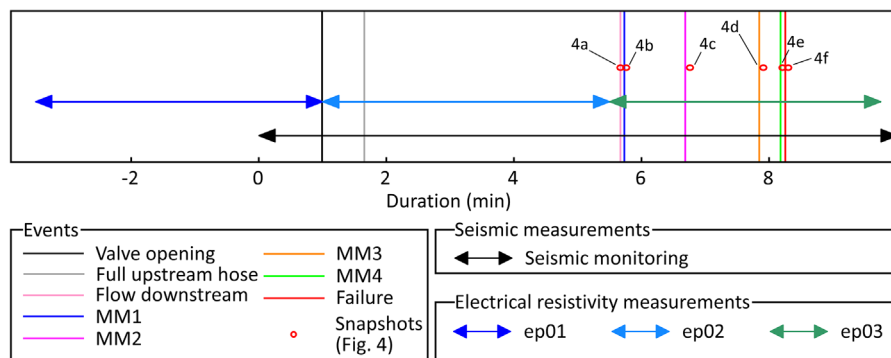


Figure 3 Chronological framework of the geophysical measurements along with the observed events. MM: mass movement.

changes (Larose *et al.*, 2015). However, considering the high velocity in the concrete with respect to the dimension of the experimental setup and to the sampling frequency, the cross-correlation between couples of geophones eventually resembles autocorrelation. It was then chosen to auto-correlate signals recorded on the geophone located above the soil sample. Seismic signals were first cut in 2-s-long windows. They were then standardized (subtraction of the mean and normalization by the standard deviation of the 2-s-long samples) and further auto-correlated. Classical ambient seismic noise studies imply a spectral whitening of the seismic recordings to avoid the correlation being dominated by a particular source (Bensen *et al.*, 2007). The cross-correlation of successive time windows gives insight into the evolution of the Green's functions and of the changes in the medium. Contrary to these studies (e.g., Planès *et al.*, 2016), an active and repetitive source was introduced, in the form of a controlled leak located upstream. That source was energetic enough to be recorded by the geophones and, hence, to monitor the evolution of the experiment.

RESULTS

A chronological framework of the geophysical measurements and the visual observations is presented in Figure 3. The time reference $t = 0$ coincides with the start of the seismic monitoring and will be the same throughout the following. The experiment started with ERT measurement ep01 at time $t = -3.5$ min. Seismic monitoring started around 1 min before the end of ep01. At the end of ep01, the valve was opened and water started to flow into the soil sample. Period ep02 started at the same time ($t = 1$ min) and lasted around 4.5 min. Finally, ep03 lasted around 4.25 min and was acquired during the occurrence of collapses and/or slides (which will be further referred to as mass movements, MM) and, eventually, the complete failure. Period ep03 ended at time $t = 9.75$ min,

which is around 1.25 min after the complete failure of the soil sample.

Video monitoring

Figure 4 shows 6 different frames extracted from the video-recorded downstream, taken at specific times. Snapshot a (Fig. 4a) was taken at 5.67 min when the first drop of water appeared downstream. At this time, the water pipe was established, although there was no measurable water flow. Snapshot b (Fig. 4b) was taken at 5.76 min, just after the first mass movement (MM1) event that occurred from 5.7 min to 5.76 min and which is evidenced in the snapshot. There was no noticeable change in the water flow following this MM. Snapshot c (Fig. 4c) was taken at 6.76 min, just after the second mass movement (MM2) event that occurred from 6.61 min to 6.76 min and which is also visible in the snapshot. Once again, there was no noticeable change in the water flow following MM2. However, it showed a significant amount of mud, suggesting that the amount of water in the soil sample had increased with respect to the conditions at the time of MM1. Snapshot d (Fig. 4d) was taken at 7.91 min, just after MM3, which occurred from 7.78 min to 7.91 min (i.e., roughly 8 s of slow mass movement) and which is evidenced in the snapshot. Although a small quantity of water is visible in the image, again there was no noticeable change in the water flow following this mass movement. The snapshot in Figure 4c was taken at time 8.21 min, just after MM4 which occurred from 8.15 min to 8.21 min (i.e. roughly 8 s of a slow mass movement, with a progradation of the soil visible in the snapshot). At this time, an increase in the water flow was observed following this mass movement. Finally, snapshot f (Fig. 4f) was taken at time 8.3 min, when the complete failure of the soil sample was reached, together with a free water flow. The 5.4 s duration between snapshots e and f suggests an

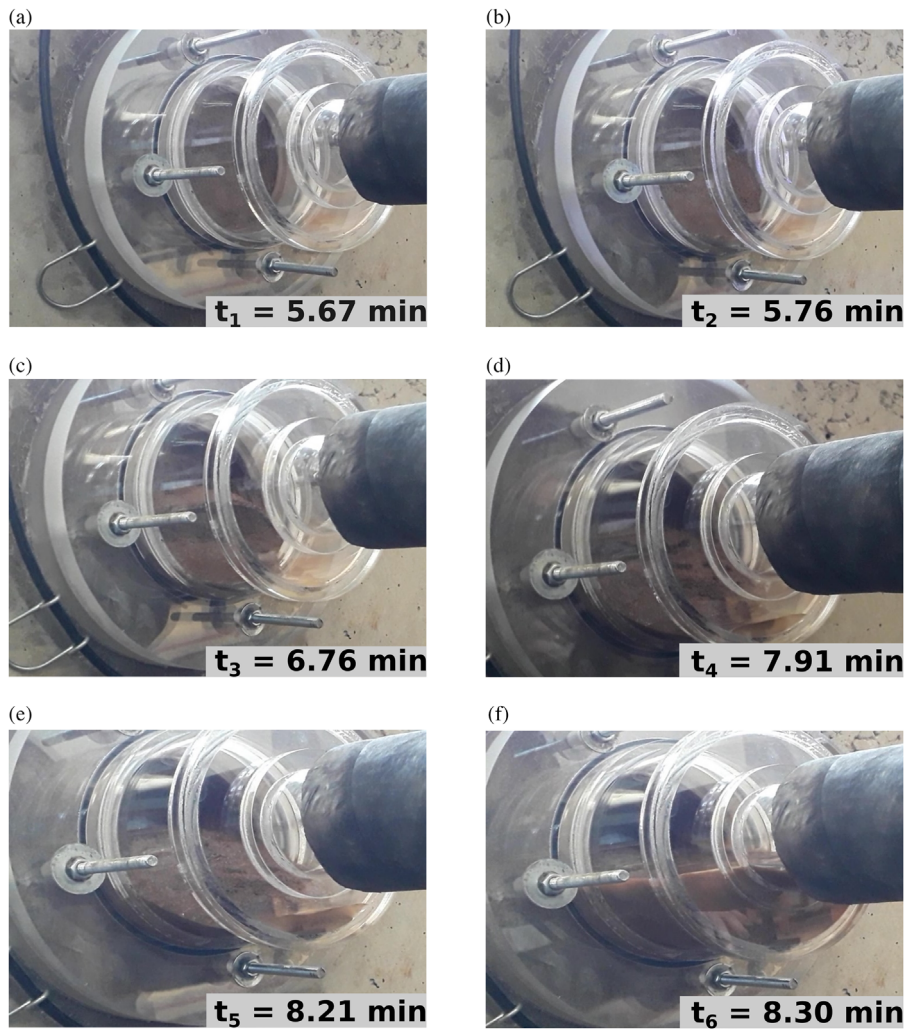


Figure 4 Captions taken from the video of the camera mounted downstream during the seepage of water in the soil sample. (a) The water reaches the downstream. (b–e) Mass movements MM1 to MM4, respectively. (f) Failure of the soil sample allowing water to flow freely. See Figure 3 for the location of the events on the timeframe.

acceleration of the erosion process towards the failure of the soil sample.

Electrical resistivity imaging and monitoring

Figure 5(a) shows the mesh adopted for the inversion of synthetic and experimental measurements along with the location of the seepage zone and the electrodes, and statistical results are detailed in Table 1. Figure 5(b) shows the resistivity distribution of the synthetic measurements with the complete sequence (74 measurements, above) and the optimized sequence (37 measurements, below). The image is a 2D slice extracted from the 3D volume and passing through the vertical plane defined by the location of the electrodes (“slice” in Fig. 5a). Statistical results show that inversion converged to-

Table 1 Statistical results of synthetic and experimental inversions of electrical resistivity data. RRMSE: relative root mean square error

Dataset	Iterations (#)	χ^2	RRMSE (%)
Synthetic computations			
74 measurements	4	1.5	3.7
37 measurements	4	1.2	3.4
Inversion of experimental data			
ep01	2	0.9	9.3
ep02	3	3.4	5
ep03	3	5	6

wards satisfactory results after 4 iterations ($\chi^2 \approx 1-1.5$ and RRMSE < 5%). The examination of the figure shows that

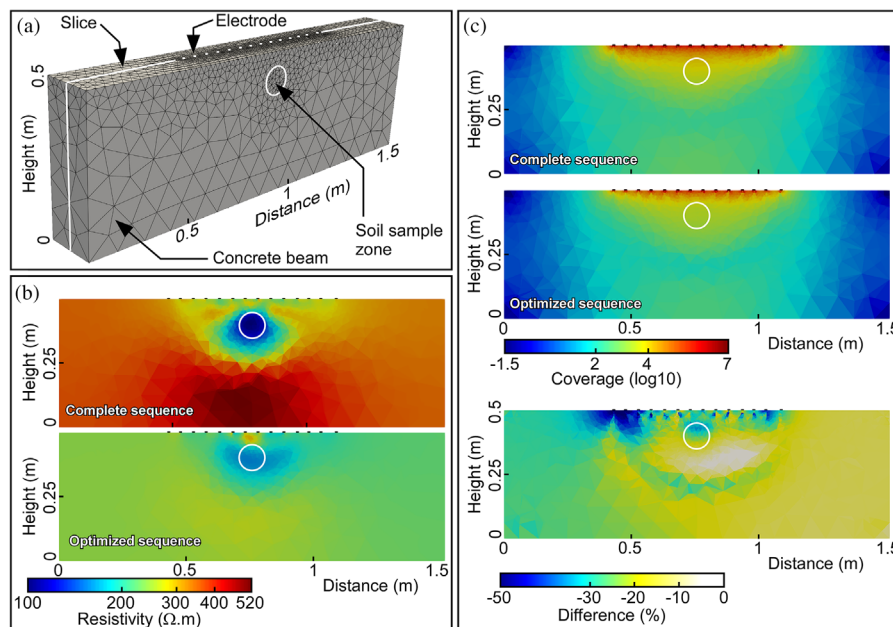


Figure 5 Synthetic results with the complete (74 measurements) and the optimized (37 measurements) sequences. (a) The mesh used for inversion along with the location of the slice shown in Figure 8(b, c). (b) Resistivity slices from the 3D models. (c) Coverage slices from the 3D models along with the difference, expressed in percent, between the complete and optimized sequences. All slices pass through the vertical plane defined by the line of electrodes.

Table 2 Inversion results of the synthetic dataset. Resistivity of the concrete and of the soil sample in the numerical model were initially set to 500 and 300 $\Omega.m$, respectively

	Resistivity of the concrete ($\Omega.m$)			Resistivity of the soil ($\Omega.m$)		
	Min.	Max.	Average $\pm 1\sigma$ (volume and coverage-weighted)	Min.	Max.	Average $\pm 1\sigma$ (volume and coverage-weighted)
Synthetic dataset						
74 measurements	130	530	420 \pm 25	100	120	110 \pm 5
37 measurements	160	310	270 \pm 60	150	190	160 \pm 5

considering the particular geometry of the experiment and the 2D acquisition setup, the complete sequence provides a fair image of the studied structure along with, however, average resistivity (420 and 110 $\Omega.m$ in the concrete and the soil, respectively; Table 2) different from the model (500 $\Omega.m$ and 300 $\Omega.m$ in the concrete and the soil, respectively). Furthermore, the limit between concrete and soil is not clearly located. Stronger decoupling between the two zones was tested. On the one hand, it allowed to better distinguish these two zones. On the other hand, it led to unsatisfactory statistical results along with resistivity values far away from the model. It was then chosen to keep a decoupling of 50% to get more realistic resistivity values. Compared to the complete sequence (real duration of around 8.5 min), the optimized sequence (real duration of around 4 min) provides a degraded image of the structure in terms of the location of the soil zone. Furthermore, average

resistivity values (230 $\Omega.m$ and 160 $\Omega.m$ in the concrete and the soil, respectively; Table 2) are also not in agreement with the model.

Figure 5(c) presents the coverage analysis. Coverage images of the complete and the optimized sequences appear fairly similar to the log scale. However, the relative difference between the optimized and complete sequences (bottom part of Fig. 5c) reveals a global decrease, down to -50% in the vicinity of the first electrodes along the profile. In the soil sample zone, this decrease is around -15% in the bottom part and decreases down to around -40% in the upper part. This global decrease is not surprising considering the decrease in the number of experimental measurements by a factor of two. It suggests that other optimizing techniques could have been tested, such as the Compare R method, which aims at optimizing the resolution matrix (Wilkinson *et al.*, 2006). It also

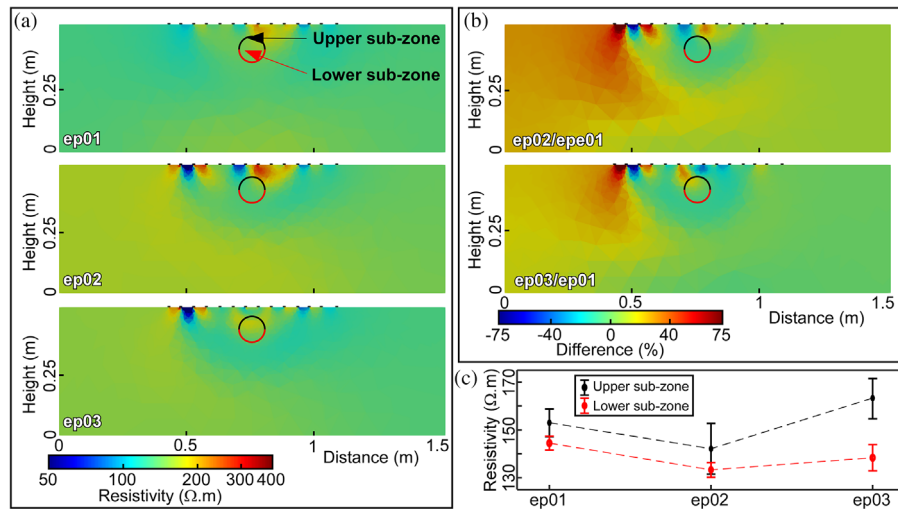


Figure 6 Experimental electrical resistivity tomography results. (a) Tomographic images for measurements ep01 to ep03 from top to bottom, respectively. (b) Resistivity difference of tomograms ep02 and ep03 with respect to ep01. (c) Evolution of the average resistivity of the upper (in black) and lower (in red) sub-zone. Error bars correspond to the standard deviation. These sub-zones are indicated in Figure 6(a).

suggests that, for such short-duration measurement sequences, multi-channel resistivity meters would prevent such strong decreases in sensitivity or resolution.

The results of the inversion of experimental resistivity are shown in Table 1 and Figure 6. Average contact resistances were around 7200–7500 Ω (ep01 and ep02) and 9400 Ω (ep03). The first set of data representing the baseline before the opening of the valve is shown in Figure 6(a). In agreement with synthetic results, the soil sample zone is very poorly detected with the optimized sequence. The soil sample zone was further divided into two sub-zones, namely the upper and lower sub-zones (Fig. 6a). Figure 6(b) presents the relative resistivity differences (expressed in per cent) between, on the one hand, ep02 and ep01 and, on the other hand, ep03 and ep01. Profile ep02 was acquired when the valve was opened up until 4.5 min. This time corresponds to the water seepage in the soil sample and precedes time 5.67 min when the water reached the downstream, meaning that the sequence encompasses the major part of the saturation of the soil sample. The relative difference in Figure 6(b) shows a global increase of resistivity in the beam in the low-sensitivity zone. Then, a strong decrease (down to -75%) and increase (up to 75%) of resistivity are observed between the electrodes. These are visible in Figure 6(a) for ep02 and ep03. These strong variations could originate from contact resistances, where the saltwater injected before starting the experiment flowed in the concrete and did not allow to keep low contact resistance. Finally, Figure 6(b) shows a decrease in electrical resistivity in the soil sample zone. It highlights the increase in water content of the

sample and the partial saturation during the data acquisition time. The third data set ep03 is from 4.5 min until the failure of the soil sample. As shown in Figures 3 and 4, this duration corresponds to the time when the water reached the downstream and was followed by a series of mass movements leading to the failure. Figure 6(c) shows the evolution of the average resistivity of the 2 sub-zones. For both sub-zones, it decreases between ep02 and ep01 (-7%). This could correspond to the higher water content in the soil sample accompanying its saturation. Between ep03 and ep02, resistivity increases by $\sim 3.5\%$ and 15% for the lower and upper sub-zones, respectively. This increase could be linked to the collapse of the soil identified in the video snapshots (Fig. 4b–f) that induced the replacement of soil particles by air. However, even if these results fit the observations, large error bars suggest that these variations are poorly significant from a statistical point of view. The discrimination between lower and upper zones also appears poorly significant from the same statistical point of view.

Seismic monitoring

Figure 7 presents the passive seismic recording of geophone 3 located above the soil sample zone. Figure 7(a and b) presents the unfiltered seismogram and the corresponding time–frequency representation, respectively. The latter shows successive sequences representing the main events happening during the experiment. The time before the opening of the valve gives an insight into the background seismic noise.

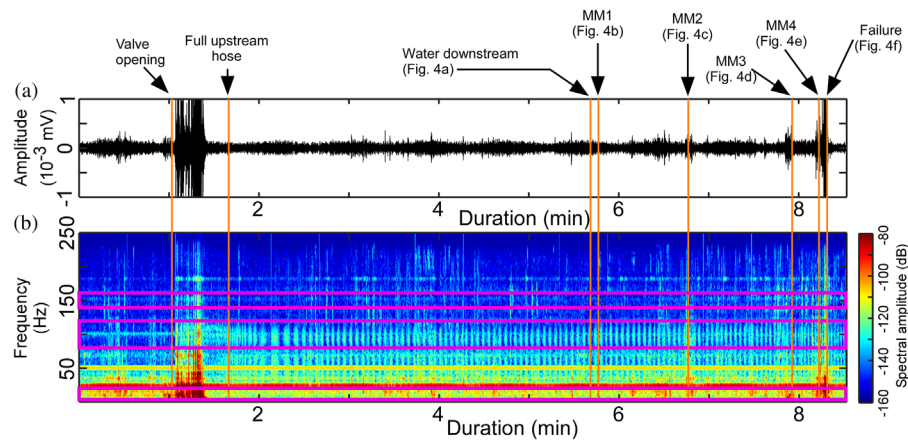


Figure 7 Seismic recordings of geophone 3 located above the soil sample zone. (a) Time series showing the main seismic events. Arrows and orange lines delimit the different phases of the experiment (valve opening, full upstream hose, water downstream, mass movements MM1 to MM4, and failure with references to the video snapshots of Figure 4). (b) Time versus frequency analysis of the seismic recordings presented in Fig 7(a). The purple rectangles show the three frequency ranges that are further analysed: 140–160 Hz, 80–120 Hz and 5–20 Hz.

High-amplitude signals are then observed from around 1.0 min to 1.5 min and correspond to the slow and progressive opening of the valve. Starting from 1.5 min and up to 7.78 min, the seismogram is formed by seismic waves very similar to the background noise. The first visible mass movement (MM1) captured by the video occurred at a time of 5.76 min. It is not associated with a clear seismic event. On the contrary, MM2 is associated with a small-amplitude seismic event, that would have gone unnoticed without the associated video recording. Finally, three other high-amplitude events are observed, namely two mass movements (MM3 and MM4) and the eventual failure, with amplitudes clearly above the background level. Several seismic events were also observed, which are associated with stronger amplitudes but not with observed events. The strong similarity of these events with what is measured before the beginning of the experiment makes it difficult to associate the seismic events with the water flow or with any rupture occurring inside the soil sample. A possible way to discriminate what is related to the environment of the experiment from what is truly related to the physics of the experiment is to decompose the seismic signal into its different components. Figure 7(b) presents the spectrogram of the seismogram up to 250 Hz (the Nyquist frequency). In this time versus frequency representation of the seismic signal, it is easier to identify the prominent features of the experiment. At the first glance, the most energetic and dominant feature of the spectrogram is the valve opening phase, which radiates mostly in the lower frequency range (0–50 Hz) and includes impulsive events that radiate up to the Nyquist frequency. The continuous energy in the 25, 50, 75, 100 Hz and so on are related to the electrical

power supply. The rupture and slow mass movements identified with the video recording have a seismic signature that is sometimes hardly visible in Figure 7b. MM1 is not recorded, possibly because of a very slow motion that does not radiate seismic energy. On the contrary, event MM2 is marked by a large seismic energy release visible at all frequencies. MM3 is associated with a small amplitude and long duration of the seismic signal, recorded mostly in the low-frequency range. Interestingly, the seismic signal started significantly before the video recording of the mass movement. A similar seismic signature is observed for MM4, a few seconds before the final failure that radiates throughout the entire frequency range.

At frequencies from 80 Hz to 120 Hz, the spectrogram is dominated by repetitive high energy events observed during the water seepage stage starting at around 1.5 min until the collapse of the soil sample. These events that do not appear in the baseline data are related to the water leakage at the upstream hose. Each droplet of water triggers a seismic wavefield that was recorded by all the geophones (see below for details). These external and repetitive seismic events were used as an active seismic source to investigate the soil sample and its evolution (see below). Finally, the spectrogram shows seismic events in the 150–250 Hz band that seem to be more numerous as the soil sample reaches the time of failure, suggesting that some of the events have to be related to the physics of the experiment.

To confirm this apparent acceleration of the number of seismic events as the experiment approaches the failure, it was decided to monitor their dynamics by counting them. Figure 8 presents the bandpass-filtered seismic data in the

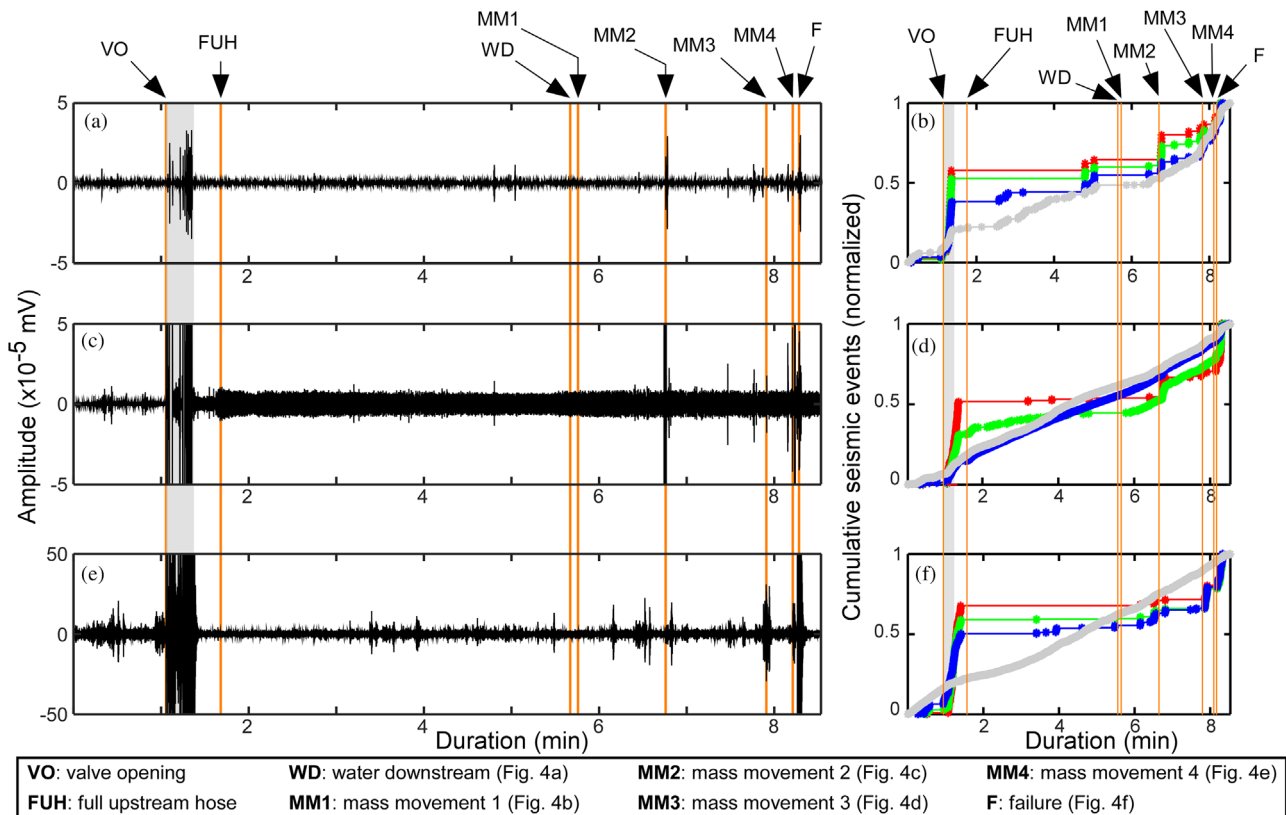


Figure 8 (a, c, and e) Seismic record of geophone 3 filtered in the 140–160, 80–120 and 5–20 Hz frequency range, respectively. Vertical orange lines indicate the different phases of the experiment (details at the bottom of the figure). The grey stripe corresponds to water movements in the tank following valve opening. (b, d and f) Cumulative number of events per class of amplitude normalized to the strongest event. Grey: normalized amplitudes between 0.1 and 0.4; blue: normalized amplitudes between 0.4 and 0.6; green: normalized amplitudes between 0.6 and 0.8; red: normalized amplitudes between 0.8 and 1.0.

three frequency bands of interest defined previously from the analysis of the spectrogram and highlighted by purple rectangles in Figure 7(b): 140–160 Hz (Fig. 8a), 80–120 Hz (Fig. 8c), and 5–20 Hz (Fig. 8e). The associated right panels (Fig. 8b, 8d and 8f, respectively) show the normalized cumulative number of seismic events detected in the seismic time series and classified by classes of amplitude. In each frequency band, the amplitude of an event was defined with respect to the strongest event of the frequency band. This normalization reveals that the strongest event of each frequency band is associated with the final failure occurring at the end of the experiment. Then, in each class of amplitude, the cumulative number of events was normalized to the total number of events of the class. This two-step normalization allows the comparison of the dynamics of the experiment in the different frequency bands. Four amplitude classes were established to differentiate the dynamics of the experiment: (1) small events between 0.1 and 0.4 represented by the grey curve;

(2) events between 0.4 and 0.6 represented by the blue curve; (3) events between 0.6 and 0.8 represented by the green curve; and, finally, (4) events larger than 0.8 represented by the red curve.

Figure 8(a and b) present the seismograms and the cumulative number of seismic events, respectively, in the frequency range 140–160 Hz. Figure 8(a) shows that besides the period of valve opening, most of the seismic events (with large amplitude) occur at the time of MM2 and after. Small-amplitude seismic events are visible from 2 min to 4 min. One stronger series of events is recorded around time 5 min. Some of these events could be related to environmental noise and, if so, their occurrence should follow a random pattern. Figure 8(b) shows that for all classes of seismic detections the pattern is not random at all. Not considering the period of valve opening, the first three minutes reveal events with small amplitudes: the grey curve increases continuously and rather slowly. Slightly before 3 min, blue class seismic events are detected, and the rate of grey class

events suddenly increases. A similar sequence occurs at 5 min, with detections in all the classes. It suggests that a large event occurred within the soil sample which was not captured by video recording. Then, the system remains extremely quiet with no detection in this band until time 6.5 min, despite the occurrence of MM1 within that period. With the water appearing downstream starts a new sequence of small grey class events at first, rapidly followed by blue and green seismic detection and a major cluster of strong events corresponding to MM2. Contrarily to the first sequence, the rate of small grey class events is sustained and even increases slightly before MM3 (7.78 min to 7.91 min). Similarly, the rate of blue, green and red classes increases until the final failure of the soil sample. The changes in rate detection observed for the different classes of events strongly suggest that most of the detections of seismic events in the 140–160 Hz frequency band are related to the physics of the soil sample evolution rather than to environmental noise. These detections suggest that the evolution of the soil sample is complex with at least one unrecorded seismic sequence at a time slightly before 5 min. This is followed by events MM1 to MM4 and, eventually, the complete failure, all time-stamped using video recording. These events show both an increase in the rate of detection and an increase in the amplitude of the events.

Figure 8(c) presents the seismogram in the 80–120 Hz frequency band. It is dominated by a small amplitude but sustained seismic activity throughout the experiment. Some stronger seismic events are visible that correspond to the unrecorded seismic sequence occurring before 5 min (see above), event MM2 and a short period preceding the failure. The small amplitude and sustained activity that dominates the record is formed by repetitions of very short-duration events that will be discussed further. Figure 8(d) presents the cumulative number of detections per class of amplitude. The grey and blue curves are particularly linear, despite some deviations at the valve opening and during some mass movements. This linear behaviour suggests, first, a nearly constant detection rate and, second, that the seismic events correspond to a background noise added to the signals. These classes of detections are much less sensitive to the soil sample evolution. Nonetheless, they will be further used to perform independent monitoring of the evolution of the soil sample. On the contrary, the green and red classes (intermediate and strong events, respectively) obey a different evolution. Shortly after the end of the valve opening phase, the number of detections in the red class is zero before increasing very weakly until event MM2. The rate of detection in the green class is slowly decreasing until the moment when water is observed downstream (5.67 min) along with

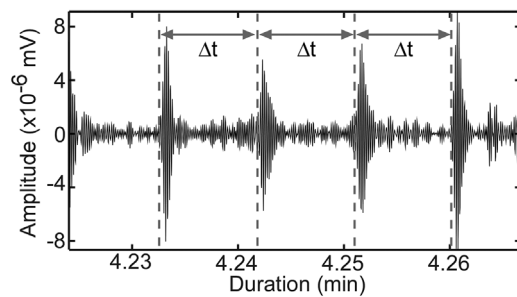


Figure 9 Impulsive, short-duration (around 0.1 s) seismic events generated each ~ 0.5 s (Δt) by a water leakage at the upstream part of the experiment and which was used as a seismic source to investigate the soil sample. The total duration shown in the figure is around 2.56 s.

event MM1 (between 5.7 min and 5.76 min), where the rate increases suddenly. The occurrence of the second event MM2 (from 6.61 min to 6.76 min) generated a bunch of strong and intermediate seismic events that are also recorded in the 140–160 Hz frequency band. Interestingly, the green class shows a sustained rate that accelerates with the occurrence of the last sequences of events MM3 (7.78 min to 7.91 min) and MM4 (8.15 min to 8.21 min) before the failure (8.3 min).

Figure 8(e) presents the record of the seismic activity filtered in the 5–20 Hz frequency range. The background seismic noise is important because it captures the steps of the experimentalists before the valve opening. Shortly after, the seismic signal is of low amplitude, with barely any strong events. The situation changes at 3 min, with the first stronger events occurring. Some of them are apparently not related to the macroscopic events recorded by the video or detected in the 140–160 Hz band. Figure 8(f) presents the cumulative number of detections per class of amplitude. The grey curve shows a nearly linear behaviour, suggesting again that these small-amplitude events are related to the seismic background noise. On the contrary, the blue, green and red curves show strongly nonlinear behaviours. The blue curve shows the first detection shortly after 3 min, rapidly followed by the green curve. Only very few events occur in these classes and none in the red class. Changes are observed between 6 and 7 min (i.e., between MM1 and MM2), with an increase in detection rate in blue, green and red classes. Interestingly, the detections precede event MM1 and stop at the time of event MM2. Then, the curves increase again shortly before events MM3, MM3 and, eventually, the final failure.

The repetitive, short-duration events shown in Figure 8(c) (grey and blue curves) are illustrated in Figure 9. The seismogram shows impulsive events (duration of around 0.1 s) occurring at intervals Δt of around 0.5 s at this moment

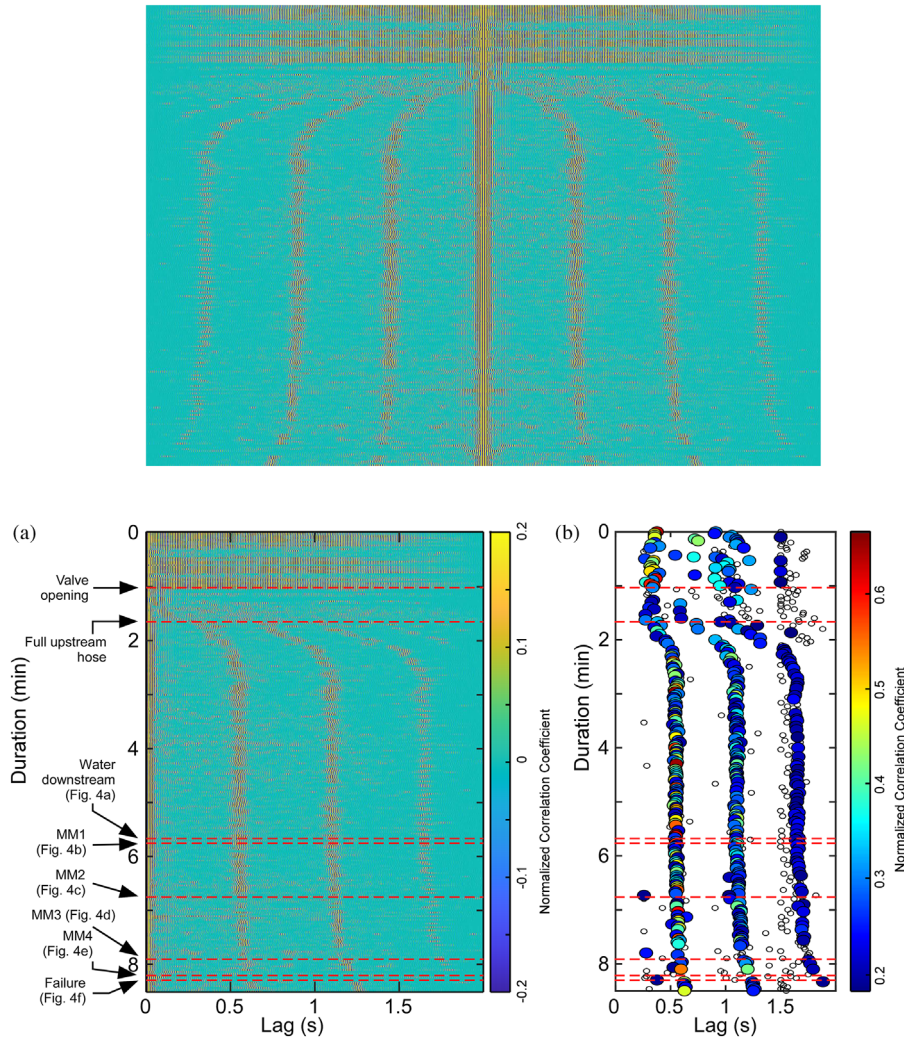


Figure 10 Autocorrelation of seismic time series recorded by geophone 3 located immediately above the soil sample zone and filtered between 80 and 120 Hz. (a) Causal part of the autocorrelation (the acausal part is symmetric). (b) Maximum cc values of each autocorrelation. cc values below 0.18 were discarded and are represented by small white-filled circles. Monitored and observed events are indicated by red dashed lines.

of the experiment. These are the records of a leakage that appeared at the upstream side of the experiment and which regularly generated water drops each 0.5 s. This *a priori* superimposed noise was used as an active seismic source. It will be further used to illustrate the changes in time required for a wavefront to scan the experimental setup (i.e., the beam and the soil sample).

The wave created by this source passes through the concrete beam and the soil sample. Any change in the medium (i.e., in the soil sample, since no change occurs in the concrete) should lead to a change in the arrival time of the seismic wave. Therefore, a correlogram was computed from the autocorrelation of successive 2-s-long seismograms of geophone 3 placed

on top of the seepage zone and filtered in the frequency range 80–120 Hz. Results are presented in Figure 10(a) under the form of the evolution of time lags as a function of the duration of the experiment and with correlation coefficients cc represented by a colour scale. For the sake of visibility, this colour scale was intentionally limited to values ranging between -0.2 and 0.2 . Before the valve opening (and the occurrence of water drop), no clear event is visible. After the valve opening, 4 main events are detected. The first one consists of the autocorrelation with its highest correlation coefficient at zero lag. Three further events are observed at average lags of around 0.5 s, 1.0 s and 1.5 s with, however, time lags that tend to increase non-linearly as a function of the duration of the experiment.

These three further events were extracted from Figure 10(a) and are presented in Figure 10(b). The 3 curves show the same trends during the experiment. First, from 1.65 min to around 3.0 min, there is an increase in the arrival times (and, hence, a decrease in the apparent velocity). This is interpreted as originating from the progressive infill of water into the soil specimen, leading to a change in its structure and the subsequent rearrangement of soil particles. It is noticeable that the slopes of the 3 curves are not identical (this is more visible in Figure 10b). This is caused by the autocorrelation process itself, where the correlation of increasing arrival times (caused by the multiple probing of the medium by the same wave) leads to progressively increasing time lags. This also explains the decrease of the correlation coefficient with the increase of the lag time as illustrated in Figure 10(b) (with genuine *cc* values): for later arrivals, the wavefront scanned the medium several times and its similarity with the first one is degraded. Second, there is a slow increase in arrival times during the water seepage stage up to the moment when water appears at the downstream. Third, as water appears downstream at 5.67 min, followed by mass movement MM1 at 5.76 min, there is a small increase in the time lag starting from 6 min. Fourth and finally, further increases in the time lag took place; they are related to the different mass movement events and the final failure. Interestingly, the increase in the time lag appears to be controlled by the different stages of this experiment that are detected in the video monitoring. This simple measure of autocorrelation reflects the changes in water content of the soil sample and the structural changes induced by the mass movements. The only varying portion of the experiment is the soil sample. It is then considered here that the concrete beam is poorly altered and interacts very little with the water.

INTERPRETATION AND DISCUSSION

Using the snapshots from the video, four stages can be identified and related to internal erosion. First, the initiation phase could be represented by the initial movement of the soil particles as shown in Figure 4(b) with the first mass movement MM1 occurring at 5.76 min, immediately after a water flow was observed downstream (Fig. 4a). This time could indicate the end of the initiation phase. Second, the continuation stage starts immediately after, with additional mass movements MM2 (Fig. 4c) and MM3 (Fig. 4d) until 8.21 min. Third, starting from this time, an increased flow of water was observed along with mass movement MM4 (Fig. 4e), suggesting the beginning of the progression phase where the pipe was

fully developed. Fourth, failure was observed at the end of the experiment (Fig. 4f).

The electrical resistivity tomography time series (Fig. 6c) show a decrease in resistivity between ep02 and ep01. This can originate from the increase in water content of the soil sample following the opening of the valve. Then ep03 shows a global increase in resistivity compared to ep01 and ep02. This can be related to the occurrence of the different mass movements MM1 to MM4 and of the final failure, leading to the replacement of soil particles by air in the sample zone. The global evolution of resistivity then appears to agree with the observed events and suggests that electrical resistivity could be suitable to monitor internal erosion experiments in the laboratory. However, the measures conducted in this work show several strong limitations. First, and due to the short time of the experiment, the single-channel resistivity metre used here is not adapted, even if it was attempted to optimize the measuring sequence using numerical modelling (Fig. 5). In other words, several physical changes occurred during one measurement sequence. Consequently, a single ERT image encompasses several events that occurred in the soil sample zone and the device used here is not able to capture the rapid evolution of the experiment. This effect, called temporal smear, has been investigated both numerically and experimentally by Rucker (2014). Second, and even if resistivity variations appear in agreement with the physical evolution observed during the experiment, the error bars associated with the data suggest that it is difficult to state whether resistivity variations are statistically significant. Several solutions can help to overcome these issues. Modern commercial resistivity metres allow multi-channel measurements (e.g., 10–12 channels for the most common recent devices). This could have allowed using more electrodes to obtain a better reconstruction of the resistivity distribution, along with faster measurement sequences. Another solution would be the use of flexible, low-cost devices, specially dedicated to laboratory experiments such as the OhmPi resistivity metre (Clément *et al.*, 2020). Finally, other optimization methods (e.g., optimizing the resolution matrix; Wilkinson *et al.*, 2006) could be tested and compared to the results originating from the optimization of the sensitivity matrix. As a conclusion for resistivity in this experiment, the method could not indicate any additional information to what was already known from visual observation concerning the internal erosion in the soil sample.

On the contrary, the continuous monitoring using passive seismic recordings permits to interpret the evolution of the soil structure during the different stages of internal erosion, where

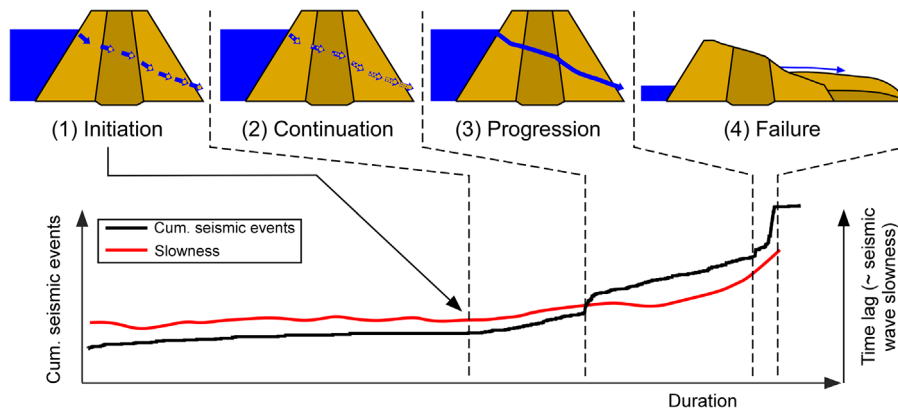


Figure 11 The different stages of internal erosion interpreted from seismic monitoring. The time lag (proportional to the apparent velocity) computed from autocorrelation is represented as a slowness (the inverse of velocity) to present a trend similar to the cumulative number of seismic events.

no visual evidence was granted. The main events that were observed during the video monitoring were detected in the seismic signals in addition to multiple events preceding and following each snapshot. These events represent changes inside the structure of the soil sample such as the rearrangement of soil particles, the transport of soil particles and small mass movements that were not identified in the video. The curve of the cumulative seismic events in Figure 8(d) (frequency range 80–120 Hz and thresholds between 0.6 and 0.8 represented by the green curve) was selected to illustrate that changes in the slope of the curve (detailed description in the section ‘Seismic monitoring’) highlight the changes corresponding to the different phases of internal erosion: (1) at 5.76 min where the initiation phase ends and the continuation phase starts; (2) at 6.76 min where high-amplitude events highlighted by a jump take place indicating the end of the continuation and the start of the progression phase; (3) at 8.21 min, another jump takes place suggesting the end of the progression phase and the start of the breach which is represented by high-amplitude events denoting the failure of the sample. The autocorrelation shown in Figure 10 also shows the changes in slopes that highlight as well the 4 stages of internal erosion: (1) a change in slope is observed at 5.76 min indicating the end of the initiation phase and the start of the continuation phase as indicated in the snapshots taken in Figure 4(b); (2) at around 7.5 min, highlighting the end of the continuation phase and the start of the progression phase; (3) at 8.30 min, the end of the progression phase and the start of the breach.

Figure 11 summarizes the seismic activity in the soil sample and its relation to the different stages of internal erosion (i.e., initiation, continuation, progression and failure). The cumulative seismic events (black curve) correspond to

the curve described above (frequency range 80–120 Hz and amplitude between 0.6 and 0.8 in Fig. 8d) where the part before 2 min was removed. The autocorrelation curve (red curve) corresponds to the time lag greater than 1.5 s in Figure 10(b). It was chosen because it shows more pronounced slope changes. Also, the time lag, proportional to the apparent seismic velocity (the greater the lag, the lower the velocity and vice-versa) was expressed in terms of slowness (the inverse of the velocity) to present a trend similar to the cumulative number of seismic events. Once again, observations before 2 min were removed to highlight the phenomenon corresponding to the evolution of the soil sample during erosion only. The two superimposed curves reveal globally similar trends with slope breaks corresponding to the identified stages of internal erosion. Changes in slope for both curves were analysed to better delineate transition zones and it must be stressed that slope breaks are less pronounced on the slowness curve than on the seismic events curve, notably at time $t = 6$ min. This can originate from high velocity in the concrete, which tends to smooth velocity changes evaluated from the autocorrelation. Experiments on more realistic structures made of soil only, and using both auto- and cross-correlation, might provide sharper changes as a function of the development of internal erosion. This also suggests that the evolution from one stage to the other has to be considered as a progressive transition rather than an abrupt change. The change from continuation to progression shows, however, a slight discrepancy between the two geophysical parameters. Nevertheless, the two parameters are in good agreement and suggest they are both suitable to detect changes in soil samples subject to internal erosion in a laboratory experiment. Moreover, it appears that in this experiment, seismic monitoring allows the detection

of early stages of internal erosion, namely initiation and continuation.

The present results are difficult to compare to previous research since very little passive seismic monitoring of earth dams has been reported so far. On the IJkdijk experiment in the Netherlands, Rittgers *et al.* (2015) successfully located acoustic emissions at depths that were associated with the development of sand/water boils. Similarly, Bièvre *et al.* (2017) were able to locate seepage a few metres below the crest of a real earth dam. In this work, it was not possible because of a too high seismic velocity in the concrete, preventing variable travel times to be retrieved from the cross-correlation of the 5 geophones initially set up. Planès *et al.* (2016) used passive seismic interferometry but started the experiment at the progression stage by artificially creating a pipe. Results from the present work show a decrease in the apparent seismic velocity (estimated from autocorrelation) as internal erosion develops. This is in agreement with their findings, which showed a decrease in seismic velocity (from cross-correlation) as internal erosion develops. Moreover, the results of this study suggest that seismic monitoring, using either acoustic emission or interferometry, is suitable to detect early stages of internal erosion. However, one question concerning the frequency band in which internal erosion radiates arises. In this work, energy is observed at frequencies greater than 100 Hz. On the IJkdijk field-scale experiment, Rittgers *et al.* (2015) and Planès *et al.* (2016) observed spikes of energy above 100 Hz, which, however, they both attributed to anthropogenic noise originating from machines operating on site. In a laboratory experiment using both active and passive acoustic techniques for internal erosion characterization, Lu and Wilson (2012) observed acoustic emissions associated with a waterflow within a 6 mm diameter soil pipe contained in a soil bed. The associated frequency band ranged between 200 Hz and 6000 Hz. On a real site, Bièvre *et al.* (2017) observed seismic energy at a frequency of around 25 Hz that was interpreted as originating from the water flow inside the dam. However, the frequency sampling used in this work (250 Hz) does not allow analysing the frequency content above 125 Hz. The question regarding the frequency content of the water flow associated with internal erosion within an earth dam remains thus an open question.

The encouraging results obtained in this work have, however, to be confirmed, notably by conducting experiments at a larger scale, using analogous models more representative of earth dams. Also, the methodology has to be extended to real sites where piping occurs at depth, typically several metres, to evaluate its ability to detect early stages of internal erosion. For testing and research purposes, experiments can

be conducted using sets of up to a few tens of classical geophones. However, this approach cannot be used to monitor several tens to hundreds of metres of earth dams to detect early stages of internal erosion. This upscaling could be achieved using emerging techniques, such as distributed acoustic sensing, which has shown the ability of the technique to detect leakages in earth dams (Mateeva *et al.*, 2013; Abbasimaedeh *et al.*, 2021). Finally, such real sites are likely to exhibit much higher background noise than in the laboratory. Consequently, early stages of internal erosion will most probably exhibit amplitudes of the same order of magnitude as background noise. Extracting relevant information will then be challenging. It could be achieved using machine learning/artificial intelligence tools (e.g., Fisher *et al.*, 2017), which are increasingly used to extract and cluster observations from various time series.

CONCLUSIONS

A controlled laboratory experiment consisting of a pipe embedded into an inert concrete beam was designed to monitor early stages of internal erosion. The temporal evolution of the soil sample submitted to a constant hydraulic head was monitored with cameras to time-stamp the evolution of the seepage from saturation up to failure. Electrical resistivity was monitored with a single-channel device. Results did not show any additional information about the internal erosion process due to the quickness of the experiment. Consequently, not enough observation was provided to monitor the changes in the soil structure. The ability of electrical parameters to capture such rapid changes in a laboratory experiment could be increased by testing other approaches. First, increasing the number of channels would allow increasing the number of measurements, and, consequently, the resolution, while keeping relatively short durations of acquisitions. Second, other sensitive electrical parameters could be tested, such as induced polarization and spontaneous potentials.

On the contrary, the seismic monitoring provided satisfactory results. The cumulative counts of seismic events along with the variations of apparent seismic velocity approximated from autocorrelation were calibrated with video monitoring. The spectral analysis showed that distinct events occurred for specific frequency ranges, such as water flow (5–20 Hz) and mass movements (80–120 Hz), allowing to monitor the full evolution of the experiment. The seismic time series allowed to differentiate different stages: baseline, valve opening, water seepage, mass movements and failure. They reveal that the evolution of the soil sample with time is complex, nonlinear and can be subdivided into distinct episodes. Both visual

observations and seismic interpretations of the data allowed the identification of the 4 different stages of internal erosion (i.e., initiation, continuation, progression and failure). The seismic data show high-amplitude events preceding the progression phase identified in the snapshots. Hence, this experiment suggests that seismic techniques are suitable to detect changes inside the structure of the soil which may lead to failure. These preliminary and encouraging results pave the way for more realistic experiments at a larger scale.


ACKNOWLEDGEMENTS

This work benefited from grants from IRD (Institut de Recherche pour le Développement, France), LabEx OSUG@2020 (Univ. Grenoble Alpes, France), the federative structure VOR (Vulnérabilité des Ouvrages aux Risques, Univ. Grenoble Alpes, France), USAID Partnerships for Enhanced Engagement in Research (PEER) Program (Project 2–514: ‘Health assessment of earth dams in Lebanon: towards sustainable development’), and internal grants from ISTERre (Institut des Sciences de la Terre, Univ. Grenoble Alpes, France). G. Bièvre and C. Voisin are part of LabEx OSUG@2020 (ANR10604 LABX56). The authors thank the associate editor and the three reviewers who greatly helped to enhance the quality of this manuscript.

DATA AVAILABILITY STATEMENT

The data that support the findings of this study are available from the corresponding author upon reasonable request.

ORCID

Grégory Bièvre  <https://orcid.org/0000-0002-6382-2824>

REFERENCES

- Abbasimaedeh, P., Tatin, M., Lamour, V., Vincent, H., Bonelli, S. and Garandet, A. (2021) On earth dam leak detection based on using fiber-optic distributed temperature sensor (case study: Canal embankment on the Rhône River, France). In: An, J., Zhang, J. and Xie, J. (Eds.) *New Approaches of Geotechnical Engineering: Soil Characterization, Sustainable Materials and Numerical Simulation, GeoChina 2021. Sustainable Civil Infrastructures*. Cham: Springer, pp. 44–57. https://doi.org/10.1007/978-3-030-79641-9_4
- ASTM (2014) Standard test methods for specific gravity of soil solids by water pycnometer. Standard D854-14. *ASTM International, West Conshohocken, USA*. <https://doi.org/10.1520/D0854-14>
- ASTM (2017) Standard test methods for particle-size distribution (gradation) of soils using sieve analysis. Standard D6913/D6913M-17. *ASTM International, West Conshohocken, USA*. https://doi.org/10.1520/D6913_D6913M-17
- Bensen, G.D., Ritzwoller, M.H., Barmin, M.P., Levshin, A.L., Lin, F., Moschetti, M.P., et al. (2007) Processing seismic ambient noise data to obtain reliable broad-band surface wave dispersion measurements. *Geophysical Journal International*, 169, 1239–1260. <https://doi.org/10.1111/j.1365-246X.2007.03374.x>
- Bièvre, G., Jongmans, D., Lebourg, T. and Carrière, S. (2021) Electrical resistivity monitoring of an earthslide with electrodes located outside the unstable zone (Pont-Bourquin landslide, Swiss Alps). *Near Surface Geophysics*, 19, 225–239. <https://doi.org/10.1002/nsg.12145>
- Bièvre, G., Lacroix, P., Oxarango, L., Goutaland, D., Monnot, G. and Fargier, Y. (2017) Integration of geotechnical and geophysical techniques for the characterization of a small earth-filled canal dyke and the localization of water leakage. *Journal of Applied Geophysics*, 139, 1–15. <https://doi.org/10.1016/j.jappgeo.2017.02.002>
- Bièvre, G., Oxarango, L., Günther, T., Goutaland, D. and Massardi, M. (2018) Improvement of 2D ERT measurements conducted along a small earth-filled dyke using 3D topographic data and 3D computation of geometric factors. *Journal of Applied Geophysics*, 153, 100–112. <https://doi.org/10.1016/j.jappgeo.2018.04.012>
- Clément, R., Fargier, Y., Dubois, V., Gance, J., Gros, E. and Forquet, N. (2020) OhmPi: an open source data logger for dedicated applications of electrical resistivity imaging at the small and laboratory scale. *HardwareX*, e00122. <https://doi.org/10.1016/j.ohx.2020.e00122>
- Clément, R. and Moreau, S. (2016) How should an electrical resistivity tomography laboratory test cell be designed? Numerical investigation of error on electrical resistivity measurement. *Journal of Applied Geophysics*, 127, 45–55. <https://doi.org/10.1016/j.jappgeo.2016.02.008>
- Clements, T. and Denolle, M.A. (2018) Tracking groundwater levels using the ambient seismic field. *Geophysical Research Letters*, 45, 6459–6465. <https://doi.org/10.1029/2018GL077706>
- Fell, R. and Fry, J.-J. (2007) The state of the art of assessing the likelihood of internal erosion of embankment dams, water retaining structures and their foundations. In: Fell, R. and Fry, J.-J. (Eds.) *Internal Erosion of Dams and Their Foundations*. New York: CRC Press.
- Fell, R., MacGregor, P., Stapledon, D., Bell, G. and Foster, M. (2015) *Geotechnical Engineering of Dams*. New York: CRC Press/Balkema.
- Fell, R., Wan, C.F., Cyganiewicz, J. and Foster, M. (2003) Time for development of internal erosion and piping in embankment dams. *Journal of Geotechnical & Geoenvironmental Engineering*, 129, 307–314. [https://doi.org/10.1061/\(ASCE\)1090-0241\(2003\)129:4\(307\)](https://doi.org/10.1061/(ASCE)1090-0241(2003)129:4(307))
- Fisher, W.D., Camp, T.K. and Krzhizhanovskaya, V.V. (2017) Anomaly detection in earth dam and levee passive seismic data using support vector machines and automatic feature selection. *Journal of Computational Science*, 20, 143–153. <https://doi.org/10.1016/j.jocs.2016.11.016>
- Foster, M., Fell, R. and Spannagle, M. (2000a) The statistics of embankment dam failures and accidents. *Canadian Geotechnical Journal*, 37, 1000–1024. <https://doi.org/10.1139/t00-030>

- Foster, M., Fell, R. and Spannagle, M. (2000b) A method for assessing the relative likelihood of failure of embankment dams by piping. *Canadian Geotechnical Journal*, 37, 1025–1061. <https://doi.org/10.1139/cgj-37-5-1025>
- Foster, M.A. and Fell, R. A framework for estimating the probability of failure of embankment dams by internal erosion and piping, using event tree methods. (1999) *UNICIV Rep. No. R-377*, Univ. of New South Wales, Sydney, Australia.
- Foster, M.A., Fell, R. and Spannagle, M. (1998) Analysis of embankment dam incidents. *UNICIV Rep. No. R-374*, University of New South Wales, Sydney, Australia.
- Foti, S., Hollender, F., Garofalo, F., Albarello, D., Asten, M., Bard, P.-Y., *et al.* (2018) Guidelines for the good practice of surface wave analysis: a product of the InterPACIFIC project. *Bulletin of Earthquake Engineering*, 16, 2367–2420. <https://doi.org/10.1007/s10518-017-0206-7>
- Garambois, S., Voisin, C., Romero Guzman, M.A., Brito, D., Guillier, B. and Réfloch, A. (2019) Analysis of ballistic waves in seismic noise monitoring of water table variations in a water field site: added value from numerical modelling to data understanding. *Geophysical Journal International*, 219, 1636–1647. <https://doi.org/10.1093/gji/ggz391>
- Graham, W.J. (1999) A procedure for estimating loss of life caused by dam failures. Tech Report No DSO-99-06, United States Bureau of Reclamation, Washington DC, USA.
- Gunn, D.A., Chambers, J.E., Dashwood, B.E., Lacinska, A., Dijkstra, T., Uhlemann, S., *et al.* (2018) Deterioration model and condition monitoring of aged railway embankment using non-invasive geophysics. *Construction and Building Materials*, 170, 668–678. <https://doi.org/10.1016/j.conbuildmat.2018.03.066>
- Günther, T., Rücker, C. and Spitzer, K. (2006) Three-dimensional modelling and inversion of DC resistivity data incorporating topography – II. Inversion. *Geophysical Journal International*, 166, 506–517. <https://doi.org/10.1111/j.1365-246X.2006.03011.x>
- Hirose, T., Nakahara, H. and Nishimura, T. (2017) Combined use of repeated active shots and ambient noise to detect temporal changes in seismic velocity: Application to Sakurajima volcano, Japan. *Earth, Planets and Space*, 69, 42. <https://doi.org/10.1186/s40623-017-0613-7>
- ICOLD (2001) *Tailings dams risk of dangerous occurrences. Lessons learnt from practical experiences*. ICOLD Bulletin, 121, International Commission on Large Dams, ICOLD, Paris, France.
- ICOLD (2017) *Internal erosion of existing dams, levees and dikes, and their foundations*. ICOLD Bulletin, 164, International Commission on Large Dams, ICOLD, Paris, France.
- Koerner, R.M., McCabe, W.M. and Baldivieso, L.F. (1981) Acoustic emission monitoring of seepage. *Journal of the Geotechnical Engineering Division*, 107, 521–526. <https://doi.org/10.1061/ajgeb6.0001414>
- LaBrecque, D.J. and Yang, X. (2001) Difference Inversion of ERT data: a fast inversion method for 3-D in situ monitoring. *Journal of Environmental and Engineering Geophysics*, 6, 83–89. <https://doi.org/10.4133/JEEG6.2.83>
- Larose, E., Carrière, S., Voisin, C., Bottelin, P., Baillet, L., Guéguen, P., *et al.* (2015) Environmental seismology: what can we learn on earth surface processes with ambient noise?. *Journal of Applied Geophysics*, 116, 62–74. <https://doi.org/10.1016/j.jappgeo.2015.02.001>
- Lu, Z. and Wilson, G.V. (2012) Acoustic measurements of soil pipeflow and internal erosion. *Soil Science Society of America Journal*, 76, 853–866. <https://doi.org/10.2136/sssaj2011.0308>
- Mateeva, A., Lopez, J., Mestayer, J., Wills, P., Cox, B., Kiyashchenko, D., *et al.* (2013) Distributed acoustic sensing for reservoir monitoring with VSP. *The Leading Edge*, 32, 1278–1283. <https://doi.org/10.1190/tle32101278.1>
- Morales-Nápoles, O., Delgado-Hernández, D.J., De-León-Escobedo, D. and Arteaga-Arcos, J.C. (2014) A continuous Bayesian network for earth dams' risk assessment: methodology and quantification. *Structure and Infrastructure Engineering*, 10, 589–603. <https://doi.org/10.1080/15732479.2012.757789>
- Olivier, G., Brenguier, F., de Wit, T. and Lynch, R. (2017) Monitoring the stability of tailings dam walls with ambient seismic noise. *The Leading Edge*, 36, 350a1–350a6. <https://doi.org/10.1190/tle36040350a1.1>
- Planès, T., Mooney, M.A., Rittgers, J.B.R., Parekh, M.L., Behm, M. and Snieder, R. (2016) Time-lapse monitoring of internal erosion in earthen dams and levees using ambient seismic noise. *Géotechnique*, 66, 301–312. <https://doi.org/10.1680/jgeot.14.P.268>
- Rittgers, J.B., Revil, A., Planès, T., Mooney, M.A. and Koelewijn, A.R. (2015) 4-D imaging of seepage in earthen embankments with time-lapse inversion of self-potential data constrained by acoustic emissions localization. *Geophysical Journal International*, 200, 758–772. <https://doi.org/10.1093/gji/ggu432>
- Rücker, C., Günther, T. and Spitzer, K. (2006) Three-dimensional modelling and inversion of DC resistivity data incorporating topography – I. Modelling. *Geophysical Journal International*, 166, 495–505. <https://doi.org/10.1111/j.1365-246X.2006.03010.x>
- Rucker, D. (2014) Investigating motion blur and temporal aliasing from time-lapse electrical resistivity. *Journal of Applied Geophysics*, 111, 1–13. <https://doi.org/10.1016/j.jappgeo.2014.09.010>
- Silva Rotta, L.H., Alcântara, E., Park, E., Galante Negri, R., Nina Lin, Y., Bernardo, N., *et al.* (2020) The 2019 Brumadinho tailings dam collapse: possible cause and impacts of the worst human and environmental disaster in Brazil. *International Journal of Applied Earth Observation and Geoinformation*, 90, 102119. <https://doi.org/10.1016/j.jag.2020.102119>
- Sjödahl, P., Dahlin, T. and Johansson, S. (2009) Embankment dam seepage evaluation from resistivity monitoring data. *Near Surface Geophysics*, 7, 463–474. <https://doi.org/10.3997/1873-0604.2009023>
- Terzaghi, K., Peck, R. and Gholamreza, M. (1996) *Soil Mechanics in Engineering Practice*. New York: John Wiley & Sons.
- Van Beek, V.M., Bezuijen, A. and Sellmeijer, H. (2013). 3. In: Bonelli, S. and Nicot, F. (Eds.) *Backward Erosion Piping*. New York: John Wiley & Sons, Ltd.
- Voisin, C., Garambois, S., Massey, C. and Brossier, R. (2016) Seismic noise monitoring of the water table in a deep-seated, slow-moving landslide. *Interpretation*, 4, SJ67–SJ76. <https://doi.org/10.1190/INT-2016-0010.1>
- Wahl, T., Regazzoni, P.-L. and Erdogan, Z. (2008) Determining erosion indices of cohesive soils with the hole erosion test and jet erosion test. *United States Bureau of Reclamation, Denver, USA*.

- Wan, C.F. and Fell, R. (2004) Investigation of rate of erosion of soils in embankment dams. *Journal of Geotechnical and Geoenvironmental Engineering*, 130, 373–380. [https://doi.org/10.1061/\(ASCE\)1090-0241\(2004\)130:4\(373\)](https://doi.org/10.1061/(ASCE)1090-0241(2004)130:4(373))
- Weller, A., Lewis, R., Canh, T., Möller, M. and Scholz, B. (2014) Geotechnical and geophysical long-term monitoring at a levee of Red River in Vietnam. *Journal of Environmental & Engineering Geophysics*, 19, 183–192. <https://doi.org/10.2113/JEEG19.3.183>
- Wilkinson, P.B., Meldrum, P.I., Chambers, J.E., Kuras, O. and Ogilvy, R.D. (2006) Improved strategies for the automatic selection of optimized sets of electrical resistivity tomography measurement configurations. *Geophysical Journal International*, 167, 1119–1126. <https://doi.org/10.1111/j.1365-246X.2006.03196.x>